Research Article

# Entropic and enthalpic factors determining the thermodynamics and kinetics of carbon segregation from transition metal nanoparticles

Satoru Fukuhara [a, *, 1], Kristof M. Bal [b, 1], Erik C. Neyts [b], Yasushi Shibuta [a]

[a] Department of Materials Engineering, The University of Tokyo, 7-3-1 Hongo, Bunkyo-ku, Tokyo, 113-8656, Japan
[b] Department of Chemistry, NANOlab Center of Excellence, University of Antwerp, Universiteitsplein 1, 2610, Wilrijk, Antwerp, Belgium

## ARTICLE INFO

## ABSTRACT

The free energy surface (FES) for carbon segregation from nickel nanoparticles is obtained from advanced molecular dynamics simulations. A suitable reaction coordinate is developed that can distinguish dissolved carbon atoms from segregated dimers, chains and junctions on the nanoparticle surface. Because of the typically long segregation time scale (up to μs), metadynamics simulations along the developed reaction coordinate are used to construct FES over a wide range of temperatures and carbon concentrations. The FES revealed the relative stability of different stages in the segregation process, and free energy barriers and rates of the individual steps could then be calculated and decomposed into enthalpic and entropic contributions. As the carbon concentration in the nickel nanoparticle increases, segregated carbon becomes more stable in terms of both enthalpy and entropy. The activation free energy of the reaction also decreases with the increase of carbon concentration, which can be mainly attributed to entropic effects. These insights and the methodology developed to obtain them improve our understanding of carbon segregation process across materials science in general, and the nucleation and growth of carbon nanotube in particular.

© 2020 Elsevier Ltd. All rights reserved.

## 1. Introduction

Segregation phenomena are quite important in various fields of material science and catalytic chemistry. For example, segregation of carbon atoms at grain boundaries is important for the strengthening of steel [1,2]. Segregation of carbon atoms is known as poisoning in heterogeneous catalysis, which reduces the catalyst activity [3]. Furthermore, carbon segregation itself is a part of the synthesis process of carbon materials such as graphene [4,5], carbon membranes [6] and carbon nanotube (CNT) [7,8]. Segregation is important regardless of whether it desired or not and therefore it should be properly understood and controlled. Segregation phenomena have been extensively studied by experiments and simulations from macroscopic viewpoint and benefits from previous studies can be achieved from the phase diagrams [9,10].

It is not straightforward to expand the phase diagram concept to the nanoscale. In case the positions of carbon atoms on grain boundaries or on surface can be defined, it is possible to

energetically calculate the stability of segregation [11] or kinetic barrier for diffusion [12] and further use this information for kinetic Monte Carlo calculations [13]. However, when the number of carbon atoms increases, the number of possible configurations will exponentially increase and taking all possible configurations into account will be difficult. In the context of CNT synthesis, several groups have carried out explicit molecular dynamics (MD) simulations in which carbon atoms were continuously added to a metal nanoparticle [14–16]. While microscopic segregation mechanisms have been observed in such simulations, they represent only a specific high flux subset of all possible pathways, due to the limited MD time scale. In a pioneering study, the phase diagram concept was extended to nanoparticles [17]. Here, it was however not always clear how to distinguish between carbon atoms that were dissolved or segregated. Furthermore, segregation is a dynamic process which is difficult to understand only from phase diagram based static picture.

In order to understand the segregation process, a suitable reaction coordinate which distinguishes dissolved from segregated carbon must be found. For example, a bond distance can be set as the reaction coordinate for a simple bond dissociation reaction, while an order parameter can be used to describe phase transition

---

* Corresponding author.
   *E-mail address:* fukuhara@mse.mm.t.u-tokyo.ac.jp (S. Fukuhara).
[1] Means equal contribution.

(i.e., solid or liquid) in the field of metallurgy [18]. Once a good approximate reaction coordinate—also referred to as a collective variable (CV)—is known, even very slow processes can then be accessed within MD time scales through the application of an enhanced sampling method such as metadynamics [19–24].

Previously, we developed CVs and a metadynamics-based approach to efficiently accelerate carbon diffusion in bulk metals [25]. Although segregation phenomena can be observed using this method, it does not directly allow to specifically target the segregated state, or to draw a free energy surface. In this study, we therefore propose a reaction coordinate that is tailored to carbon segregation. Using this reaction coordinate as a CV, we can then drive the segregation process at different carbon concentrations and temperatures, reconstruct the free energy surface, and characterize the different intermediate stages. Besides recovering the segregation thermodynamics from free energy differences, we can also analyze the kinetics of the different segregation steps from activation free energies in the framework of transition state theory [26–30].

## 2. Methodology

### 2.1. Free energy in molecular dynamics

First, we describe the method to calculate the free energy in molecular dynamics. The Gibbs free energy $G(q)$ for reaction coordinate $q$ under the conditions of NPT (the number of atoms, pressure and temperature constant) is given by the probability of appearance of $q$, $P(q)$, as

$$G(q) = -\frac{1}{\beta}\ln P(q) \tag{1}$$

where $\beta$ is $= 1/k_B T$. Here $k_B$ is the Boltzmann constant and $T$ is the temperature. The total free energy of state A, $G_A$, is calculated as

$$G_A = -\frac{1}{\beta}\ln \int_{q\in A} \exp(-\beta G(q))dq. \tag{2}$$

$P(q)$ can be calculated as

$$P(q) = Z^{-1}\int_{\mathbf{R}}\exp(-\beta V(\mathbf{R}))\delta\left[q\left(\frac{\mathbf{R}}{\lambda}\right) - q\right]d\mathbf{R} \tag{3}$$

using the partition function

$$Z = \int_{\mathbf{R}}\exp(-\beta V(\mathbf{R}))d\mathbf{R} \tag{4}$$

Here, $\mathbf{R}$ represents the configuration space of all atoms and $\lambda$ is a length unit used in the definition of the reaction coordinate. In an ergodic system, $P(q)$ can be obtained by simply recording a histogram $N$ as function of $q$ as

$$P(q) = \lim_{t\to\infty}N(q,t) = \lim_{t\to\infty}\frac{1}{t}\int_0^t\delta\left[q - q\left(\frac{\mathbf{R}(t')}{\lambda}\right)\right]dt' \tag{5}$$

when the molecular dynamics simulation is sufficiently long [23].

### 2.2. Activation free energy in molecular dynamics

Transition state theory (TST) [26–30] is a theoretical framework for calculating the rate of chemical reactions. In this theory, a transition state $q_{TS}$ is located at the dividing surface between state A and state B, and the system at the transition state is assumed to relax to state A or state B with equal probability. Under this assumption, the transition frequency $\nu^{TST}$ is defined as

$$\nu^{TST}\left(q_{TS}\right) = \lim_{t\to\infty}\frac{1}{t}\int_0^t\left|\frac{d}{dt'}H\left(q\left(\frac{\mathbf{R}(t')}{\lambda}\right) - q_{TS}\right)\right|dt' \tag{6}$$

using the time derivative of the Heaviside stepfunction $H$, i.e. the number of times the reaction coordinate crosses the transition state [28]. By calculating the time differential, the equation is transformed into

$$\nu^{TST}\left(q_{TS}\right) = \lim_{t\to\infty}\frac{1}{t}\int_0^t|\mathbf{v}\cdot\nabla q|\delta\left[q\left(\frac{\mathbf{R}(t')}{\lambda}\right) - q_{TS}\right]dt' \tag{7}$$

Here, $\mathbf{v}$ is the velocity of each atom. Using ergodicity, the time average is equivalent to the phase space average:

$$\nu^{TST}(q_{TS}) = \int_{\mathbf{v}\times\mathbf{R}}|\mathbf{v}\cdot\nabla q|\delta\left[q\left(\frac{\mathbf{R}}{\lambda}\right) - q_{TS}\right]P(\mathbf{v},\mathbf{R})d\mathbf{v}d\mathbf{R} \tag{8}$$

Writing the momentum part as $M$ and the remaining part as $P^{\ddagger}$, the equation is

$$\nu^{TST}(q_{TS}) = \frac{1}{\lambda}MP^{\ddagger}(q_{TS}) \tag{9}$$

Where

$$P^{\ddagger}(q_{TS}) = Z^{-1}\int_{\mathbf{R}}\left|\lambda\nabla q\left(\frac{\mathbf{R}}{\lambda}\right)\right|\delta\left[q\left(\frac{\mathbf{R}}{\lambda}\right) - q_{TS}\right]\exp(-\beta V(\mathbf{R}))d\mathbf{R} \tag{10}$$

and

$$M = \sqrt{\frac{2}{\pi\beta m_{\perp}}}. \tag{11}$$

Here, $m_{\perp}$ denotes the mass component perpendicular to the transition state surface. The length unit $\lambda$ is used to make the $|\lambda\nabla q(\mathbf{R}/\lambda)|$ term a dimensionless quantity [30]. $P^{\ddagger}(q_{TS})$ is similar to $P(q)$ in Eq. (3) and the difference is $|\lambda\nabla q(\mathbf{R}/\lambda)|$ term, which is generated in Eq. (7) through the time differential. In this paper, we define the activation free energy $G^{\ddagger}$ as

$$G^{\ddagger} = \min_{q_{TS}}\left(-\frac{1}{\beta}\ln P^{\ddagger}(q_{TS})\right) \tag{12}$$

and $\Delta G_A^{\ddagger}$, activation free energy from state A, as

$$\Delta G_A^{\ddagger} = G^{\ddagger} - G_A. \tag{13}$$

This type of free energy including the $|\lambda\nabla q(\mathbf{R}/\lambda)|$ term corresponds to the so-called geometric free energy [28,29]. Here, choosing $q_{TS}$ so that the activation free energy takes the minimum value corresponds to estimating the optimal transition rate based on the variational transition state theory [27]. Note that $G(q_{TS})$, which is the free energy at the transition state, does not contain the term $|\lambda\nabla q(\mathbf{R}/\lambda)|$, which is not appropriate for estimating the activation free energy because the value changes depending on how the reaction coordinate is chosen. On the other hand, $G^{\ddagger}$ does not depend on the definition of the reaction coordinate. Similar to the calculation of free energy in Eq. (5), the value in Eq. (10) can be

obtained by creating a histogram with the weights of $|\lambda \nabla q(\mathbf{R}/\lambda)|$ as

$$P^{\ddagger}\left(q_{TS}\right) = \lim_{t \to \infty} N^{\ddagger}(q_{TS}, t) = \lim_{t \to \infty} \frac{1}{t} \int_0^t \left| \lambda \nabla q\left(\frac{\mathbf{R}(t')}{\lambda}\right) \right|$$
$$\times \left| \delta \left[ q\left(\frac{\mathbf{R}(t')}{\lambda}\right) - q_{TS} \right] dt'. \tag{14}$$

The reaction rate coefficient from state A to B, $k_{AB}$, is obtained by the equation

$$k_{AB} = \frac{\nu_{AB}^{TST}}{2P_A} \tag{15}$$

where $P_A$ is the probability that the system is at state A. Using Eq. (9), Eq. (12) and Eq. (13), This equation can be rewritten as

$$k_{AB} = \frac{1}{\lambda} \sqrt{\frac{1}{2\pi\beta m_\perp}} \exp(-\beta \Delta G_A^{\ddagger}). \tag{16}$$

### 2.3. Metadynamics

Free energy and activation free energy can in principle be obtained by sampling an infinitely long time. In practice, it is difficult to obtain even an approximate value for rare events with limited computational time. In this study, metadynamics is used to improve the efficiency of sampling. In metadynamics, a bias potential in the form of Gaussian functions with width $\sigma$ and height $W$ defined as

$$V_{\text{bias}}(q,t) = \sum_{k\tau < t} W(k\tau) \exp\left[ -\frac{(q(t) - q(k\tau))^2}{2\sigma^2} \right] \tag{17}$$

is added to the free energy surface as function of reaction coordinate $q$ at every $k\tau$, where $k$ is integer and $\tau$ is the interval. The reaction coordinate is usually called the collective variable in a metadynamics context. The height $W$ is modified based on the well-tempered metadynamics [21] scheme as

$$W(k\tau) = W_0 \exp\left( -\frac{V_{\text{bias}}(q(k\tau), k\tau)}{k_B \Delta T} \right). \tag{18}$$

Here, $W_0$ is the initial height and $\Delta T$ is calculated from a bias factor $\gamma$ as

$$\gamma = \frac{T + \Delta T}{T}. \tag{19}$$

In biased simulation, values such as $P(q)$ or $P^{\ddagger}(q_{TS})$ can also be obtained by creating a histogram like in Eq. (5) or Eq. (14) with a correction for added bias. For an arbitrary $O(\mathbf{R})$, the ensemble average can be recovered [24] from the biased calculation by

$$\langle O(\mathbf{R}) \rangle_0 = \lim_{t \to \infty} \frac{1}{t} \int_0^t O(\mathbf{R}(t')) \exp(\beta V_{\text{bias}}(q) - \beta c(t')) dt'. \tag{20}$$

Here, $c(\text{t})$ is defined as

$$c(t) = \frac{1}{\beta} \ln \frac{\int_q \exp(-\beta G(q)) dq}{\int_q \exp(-\beta [G(q) + V_{\text{bias}}(q)]) dq}. \tag{21}$$

In particular, $P(q)$ can be obtained by setting $O(R) = \delta[q - q(\mathbf{R}/\lambda)]$ and creating a histogram weighted by

$$\exp(\beta V_{\text{bias}}(q) - \beta c(t)) \tag{22}$$

during the calculation. In the activation free energy case, $O(R)$ is set as $|\lambda \nabla q(\mathbf{R}/\lambda)|\delta[q(\mathbf{R}/\lambda) - q_{TS}]$ and histogram is weighted by

$$\left| \lambda \nabla q\left(\frac{\mathbf{R}}{\lambda}\right) \right| \exp(\beta V_{\text{bias}}(q) - \beta c(t)). \tag{23}$$

Note that $|\lambda \nabla q(\mathbf{R}/\lambda)|$ is already calculated when calculating the force on each atom by the bias when metadynamics is run. Fig. 1 is the conceptual diagram of the method described in section 2.1, 2.2 and 2.3.

### 2.5. Considered systems and conditions

In this work, segregation of carbon atoms from a nickel nanoparticle is examined by molecular dynamics simulation in conjunction with metadynamics. Nanoparticles containing 55 Ni atoms with 8 different numbers of carbon atoms dissolved, viz. 2, 4, 8, 10, 12, 14,16 and 20, dissolved are employed as the initial structures. Ni is chosen because it is one of the most popular catalysts used in CNT synthesis and many previous computational works targeted it as the catalyst [14,16,17,31]. The particle diameter is around 1 nm, which is consistent with the diameter of a small single-walled CNT. The nanoparticle is placed at the center of a $20 \times 20 \times 20$ Å$^3$ cubic cell. Repulsive Gaussians of height $w = 0.0043$ eV and width $\sigma = 0.05$ are employed as biasing parameters in Eq. (17). Bias potential is added at every 800 steps. A bias factor of 10 is used for the well-tempered metadynamics scheme. A repulsive wall potential is set to prevent carbon atoms from evaporating. The wall is a function of the coordination number defined for each carbon
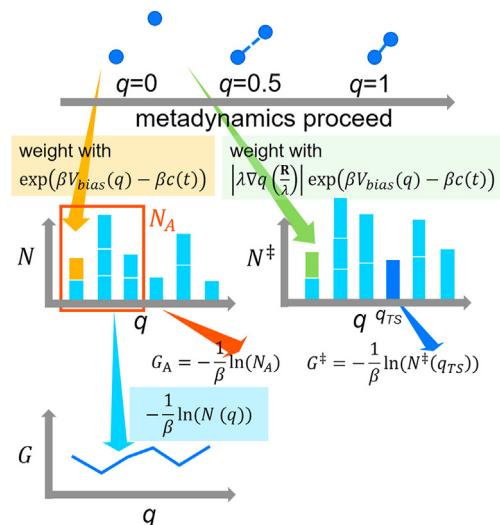


**Fig. 1.** Schematic image of calculating free energy surface: $G(q)$, free energy of state A: $G_A$ and activation free energy: $G^{\ddagger}$. These values are derived by creating weighted histograms through the metadynamics run. (A colour version of this figure can be viewed online.)

atom $i$ by

$$s_i = \sum_j \frac{1 - \left(\frac{r_{ij} - d_0}{r_0}\right)^n}{1 - \left(\frac{r_{ij} - d_0}{r_0}\right)^m} \tag{24}$$

Here, $r_{ij}$ represents the bond length between carbon atoms $i$ and nickel atom $j$, and the summation runs over all nickel atoms. The parameters are set as $d_0 = 1.0$, $r_0 = 2.0$ $n = 6$ and $m = 12$. The wall ensures that any $s_i$ does not get smaller than 1.5. A ReaxFF reactive force field [32] is employed to describe the interaction between nickel and carbon atoms, which has already been successfully applied to CNT nucleation and growth [16]. The NVT (the number of atoms, cell size and temperature constant) ensemble is sampled using a Nose-Hoover chain thermostat [33]. Note that the simulation is also at a constant pressure of 0 Pa, because the nanoparticles are placed in a vacuum. Calculations are carried out for 5 different temperatures, viz. 1200 K, 1400 K, 1600 K, 1800 K and 2000K, for all 8 carbon concentrations, thus 40 cases in total. The melting point of a nanocluster is not as unambiguously defined as in bulk, but previous simulations of $Ni_{55}$ using the same ReaxFF force field revealed that the liquid phase is more stable than the solid phase above 1000 K [34]. Therefore, the clusters in this study are all in the liquid state. The use of liquid nanoparticles also avoids poor sampling caused by high diffusion barriers in the solid state. $1.6 \times 10^7$ simulation steps are carried out for all cases with a timestep of 0.25 fs? All calculations were performed using LAMMPS [35] with the PLUMED plugin [36].

### 2.6. Reaction coordinate

Coordinates of atoms obtained from molecular dynamics calculation have $3N$ degrees of freedom, where $N$ is the number of atoms. However, it is not easy to understand a phenomenon in $3N$ dimensions when the number of atoms becomes larger. Therefore, CVs are generally introduced to compress $3N$ degrees of freedom into fewer ones for the discussion of chemical or physical transformations. Defining the CVs is of utmost importance in free energy calculations and various CVs were developed to suit a variety of applications. Order parameters are introduced for liquid-solid transformation [18] and the number of molecules in the nuclei cluster is used as CV for a nucleation of inorganic crystals [37]. Segregation is a process related to liquid-solid transformation or nucleation in the sense of having some order from the non-ordered phase, and this idea can be incorporated in the development of CVs for these applications. In this study, a CV is developed to distinguish the following two states: (i) dissolution of all carbon atoms and (ii) segregation of some carbon atoms. In order to distinguish these two states, a reaction coordinate based on the carbon−carbon coordination number is adopted. The definition of the reaction coordinate is as follows. First, for every carbon atoms $i$, its coordination number with other carbon atoms $j$ is defined as Eq. (24), in which the summation now runs over all $j \neq i$. Here, too, a switching function is used to make the coordination number a continuous quantity; its parameters are set as $d_0 = 1.2$, $r_0 = 0.6$, $n = 9$ and $m = 12$. It is designed in such a way that it can fully distinguish between different bonding patterns with other carbon atoms. When in a two-carbon system the atoms $i$ and $j$ form bonds, the value of $s_i$ (and $s_j$) becomes close to 1, and as the distance between them gets longer, the value reaches 0. Subsequently, the largest coordination number is used as the actual reaction coordinate $q$. In order to make this value continuous, the equation

$$q = \alpha \ln \sum_i \exp\left(\frac{s_i}{\alpha}\right) \tag{25}$$

is used. In this expression, we can approximate the maximum value by reducing the influence of non-maximum terms, and use $\alpha = 0.01$. With this definition, we can distinguish not only between the state with fully dissolved carbon ($q = 0$) and segregated carbon ($q \geq 1$), but also between different carbon structures as conceptually shown in Fig. 2. Note that the number of particular structures has little effect on $q$ because only the maximum coordination number as defined in Eq. (25) contributes strongly to $q$. For example, both the configuration with a single carbon dimer and multiple carbon dimer will be mapped near $q = 1$. This CV, which purely describes C−C interactions, is assumed to cover the slowest degrees of freedom in the system. This is a reasonable approximation because the nanoparticles are molten at all considered conditions. Therefore, we do not need to directly bias the Ni−Ni or Ni−C degrees of freedom.

## 3. Results and discussion

### 3.1. Free energy surface with respect to the reaction coordinate

Fig. 3 shows the free energy with respect to reaction coordinate at 1200 K calculated by metadynamics. As mentioned in Section 3.2, the reaction coordinate takes the maximum value of the coordination number. Therefore, the state of $q = 0$ represents the case with no bonds between carbon atoms. The states of $q = 1, 2$ and 3 represent the cases with carbon dimer, carbon chains with 3 or more atoms and triple junction, respectively. Broadening in the peaks is caused by the switching function employed in the definition of the reaction coordinate. The center of peaks takes a larger value than the exact position of 1, 2 and 3 because carbon atoms without bonds also contribute a little to the coordination number. It can be seen from the figure that the state of $q = 0$ (i.e. no dimer formed) is more stable when the number of carbon atoms in the nanoparticle is two. However, the peak at $q = 1$ becomes more stable as the number of carbon atoms increases and it becomes more stable than the peak at $q = 0$ when the number of carbon atoms is twenty. This indicates that the state of dimer segregation is
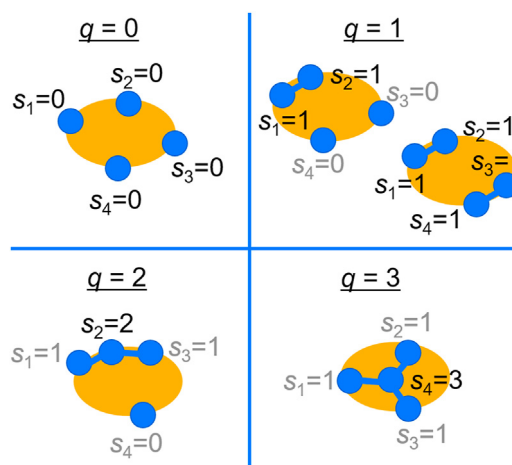


**Fig. 2.** Schematic image of reaction coordinate. Reaction coordinate ($q$) corresponds to the maximum of the coordination numbers of each carbon atom ($s_i$). Both the case with one dimer and the one with two dimers are mapped to same reaction coordinate since the maximum of the coordination numbers is employed for reaction coordinate. (A colour version of this figure can be viewed online.)
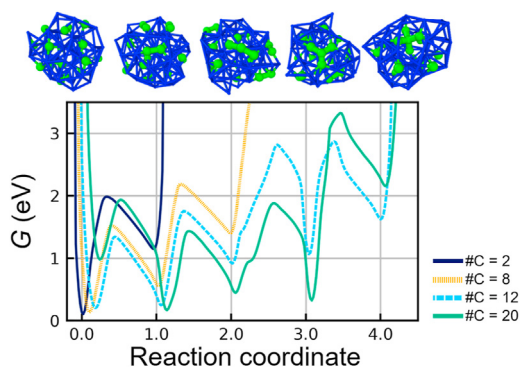
**Fig. 3.** Free energy with respect to reaction coordinate at 1200 K calculated by metadynamics. The cases with 2, 8, 12 and 20 carbons are shown. Snapshots represent typical configurations of each state in 16 carbons case. (A colour version of this figure can be viewed online.)

more stable than that of all carbon atoms dissolved in the nanoparticle. Peaks in free energy also appear at $q = 2$ and 3, which represent chain and triple junction structures, respectively. These states are crucial stages in between the initial segregation of carbon on the surface, and the formation of extended carbon nanostructures such as CNT caps. There also exists a peak at $q = 4$, which represent a sp$^3$ junction. However, this configuration is energetically not favored on the nanoparticle surface. Therefore, it is not included in the following discussion.

### 3.2. Free energy change of the reactions

From the calculated free energy surface, free energy difference between the states can be calculated using Eq. (2). Fig. 4 shows the free energy difference associated with dimer formation as a function of the carbon atom concentration. At all considered temperatures the free energy difference becomes 0 when the number of carbon atom is around 12. This concentration corresponds to the solubility limit. The dependence of the solubility limit on the temperature is small. Fig. 5 (a) shows the free energy difference between states under the different temperature conditions. The free energy of configurations containing junctions ($q = 3$) is too high to be sampled sufficiently, even with metadynamics, when the number of carbon atoms is below 10 and there is relatively little chance that at least 4 atoms get close to each other. Therefore, only systems with more than 12 carbon atoms are analyzed in this case.

The free energy is defined as $G = H - TS$ using the enthalpy $H$, temperature $T$, and entropy $S$. Assuming that the enthalpy and entropy are independent of temperature, $G(T)$ can be approximated
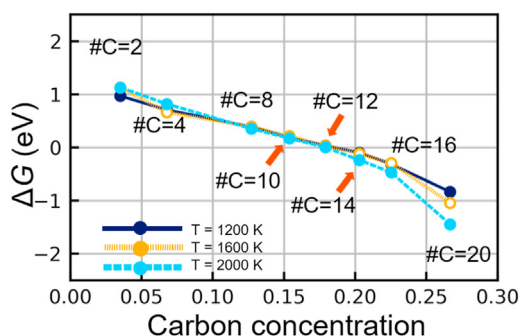


**Fig. 4.** Free energy difference of the dimer formation with respect to carbon concentration for 1200 K, 1600 K and 2000 K case. (A colour version of this figure can be viewed online.)

as a linear function, and $H$ and $S$ can be found through linear regression. The enthalpy change $\Delta H$ and entropy change $\Delta S$ between different states as obtained by fitting are shown in Fig. 5 (b) and 5 (c). It is found that, compared to the state with fully dissolved carbon, the carbon dimers become more favored both in enthalpic and entropic terms as the number of carbon atoms deposited in the nanoparticle increases. When the number of carbon atoms is near the solubility limit, i.e. 12, the entropy change become close to 0. This is the reason of the small temperature dependency of the solubility limit. When the number of carbon atoms is below 14, the dimer association enthalpy remains positive. Carbon segregation and dimer formation is therefore primarily driven by entropic factors around the solubility limit.

In contrast to dimer formation, chain formation and junction formation never become thermodynamically favored in the simulated conditions. For chain formation, the entropic term is smaller than for dimer formation at all concentrations. This means that once a dimer is formed, carbon concentration or temperature have little effect on lengthening the dimer to trimer. Junction formation appears to be enthalpically favored once chains are present when comparing the $q = 2$ and $q = 3$ states, but not entropically. Given the fairly low carbon concentrations considered, the number of carbon chains formed in the $q = 2$ state is low. For example, with 20 carbon atoms in the particle, only 2 chains at most are simultaneously observed. It is likely that if more chains are formed at the same moment with even higher carbon concentrations, the probability of junction formation between chains [15] will increase and result in a larger entropic term.

### 3.3. Activation free energy of the reactions

Fig. 6 (a) shows the activation free energy of dimer formation chain formation and junction formation under the different temperature conditions. The activation free energy is also expressed as $\Delta G^{\ddagger}_{\text{base state}} = \Delta H^{\ddagger} - T\Delta S^{\ddagger}$. Fig. 6 (b) shows the activation enthalpy change and Fig. 6 (c) shows the activation entropy change estimated by the linear fitting of the plot in Fig. 6 (a) assuming that $\Delta H^{\ddagger}$ and $\Delta S^{\ddagger}$ are independent of temperature. In the dimer formation process, the entropic term is dominant. For example, when comparing the case of 2 and 20 carbons at 1200 K, the activation enthalpy is reduced by about 0.19 eV, while the $T \times \Delta S^{\ddagger}$ term is increased by 0.70 eV. This means the enthalpy barrier in the reaction pathway does not change appreciably with the increase in the number of carbons in a reaction of a dimer formation, whereas the reaction frequency changes with the increase in the number of combinations of carbon atoms reaching the transition state. In other words, the entropic barrier for segregation is reduced with increasing carbon atom concentration. The dominance of the entropic term on the kinetics of dimer formation strongly mirrors its role in the segregation thermodynamics.

The activation energy for both chain formation and junction formation is larger than that of dimer formation for all carbon concentrations. This difference of activation energy is mainly caused by the larger enthalpic term.

### 3.4. Estimation of reaction rate

The approximate rate of reactions can be estimated using Eq. (16). For the value of $m_{\perp}$, 12, i.e. the atomic weight of carbon atom, is used with the approximation that only distance between two carbon atoms is related to the reaction. At 1200 K, the rate coefficient of dimer formation increases as $2.4 \times 10^4$ s$^{-1}$, $2.0 \times 10^7$ s$^{-1}$ and $1.2 \times 10^8$ s$^{-1}$ when the carbon number increases as 2, 12 and 20. The inverse of rate coefficient corresponds to the average time
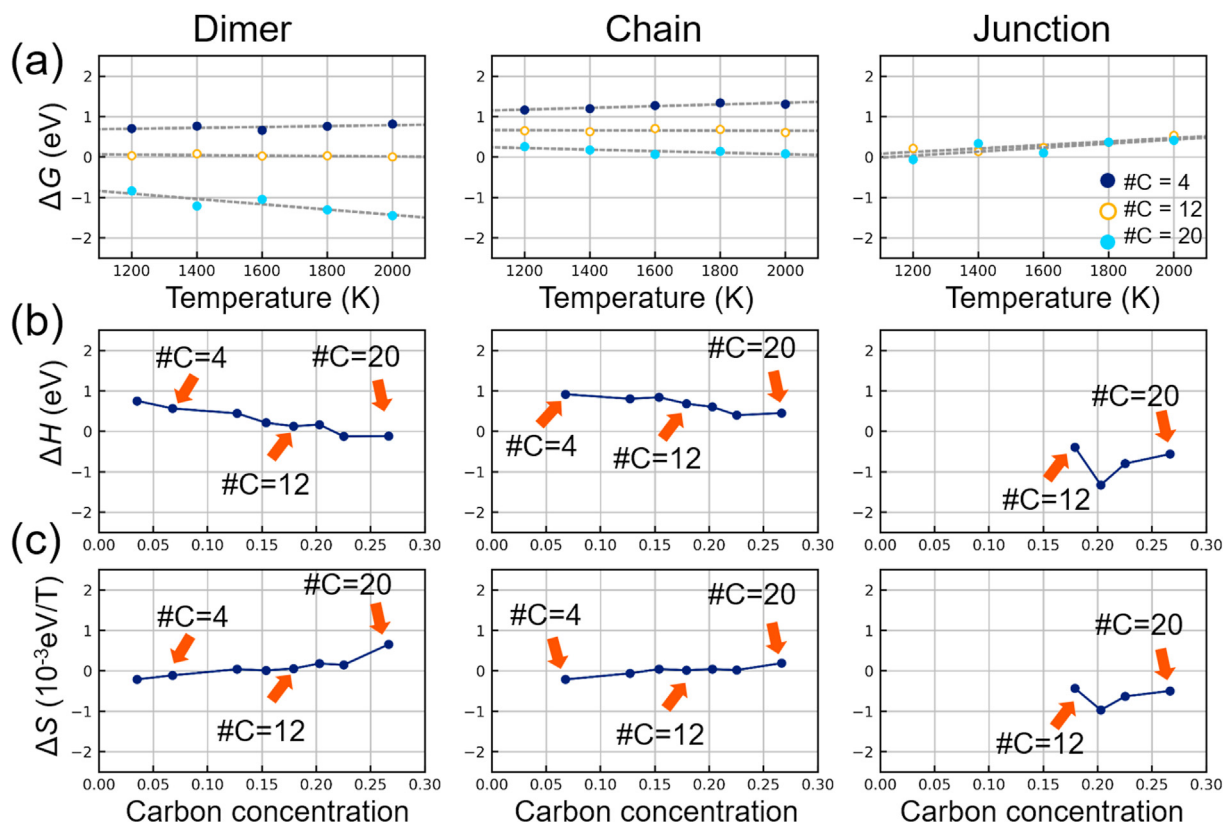
**Fig. 5.** (a) Free energy change of the reaction of dimer formation, chain formation and junction formation with respect to temperature for nanoparticles with 4, 12 and 20 carbon atoms. Dashed lines represent the fitting line for each case. (b) Enthalpy and (c) entropy change during dimer formation, chain formation and junction formation with respect to carbon concentration. (A colour version of this figure can be viewed online.)

required for single reaction and these rate coefficients mean reactions are quick enough to occur in a real-world experiment, which is usually longer than 1 s. The rate coefficients for further reactions, the formation of a carbon chain or junction, are also investigated and the result for the case of 20 carbon in 1200 K is shown in Fig. 7. Carbon chain and junction formation can be observed in the order of sub-microseconds. However, the backward reaction occurs more frequently and therefore the state with dimers is most stable at this concentration and temperature. In order to make larger carbon structure more stable, more carbon atoms are needed.

While the rates of the various carbon association processes are quite high when compared to experimental time scales, they would pose serious challenges to atomistic simulations. At the solubility limit of 12 carbon atoms, the average time of dimer formation at 1200 K is in the order of $10^{-8}$ s. This more or less constitutes the upper limit of what can be covered in a single molecular dynamics simulation, at least when no enhanced sampling methods are used. Due to time scale limitations, it has been customary to use high carbon addition rates (as fast as $ps^{-1}$), which are significantly higher than the segregation rates calculated here. This helps to explain the carbon supersaturation that has been frequently observed prior to CNT nucleation, when the number of dissolved carbon atoms is higher than during later stages in the growth process [16,38]. It might also help reconcile the much higher carbon solubility of about 25 at% in $Ni_{55}$ reported by grand canonical Monte Carlo simulations [17] which, too, can be expected to suffer from ergodicity problems when high free energy barriers are present. Our rate estimates help to underline that, in order to achieve a detailed understanding of carbon segregation from metal

nanoparticles and the initial stages of carbon nanostructure nucleation, enhanced sampling methods are invaluable tools. Standard MD simulations, even when supplemented by Monte Carlo steps [16], are bound to miss certain slow processes of the process due to their limited time scale. Moreover, by invoking the free energy surface along a suitable CV, it is possible to separate thermodynamic factors from kinetic aspects and untangle the intermediate steps of the process.

## 4. Conclusion

We have developed an atomistic simulation approach based on metadynamics to study the segregation of carbon from a metal nanoparticle. By using a reaction coordinate that can distinguish between different intermediates of the segregation process, we can not only obtain the free energy differences associated with different process steps, but also their respective free energy barriers. In addition, enthalpic and entropic contributions are extracted independently from temperature dependence of the free energy. We find that it is the entropy term that mostly controls the initial dimer formation process, while the formation of larger structures entails a more subtle balance between entropy and enthalpy. The obtained results can be used in experiments as a guideline to control the rate of carbon supply to either prevent carbon segregating from nanoparticle, or to promote the formation of carbon structures. From the computed reaction rates, it is clear that these processes are very difficult to capture reliably with standard simulation approaches.

The reaction coordinate developed in this study can be applied to segregation of other atoms from other clusters. Furthermore, the methodology is not limited to small particle sizes and it is even
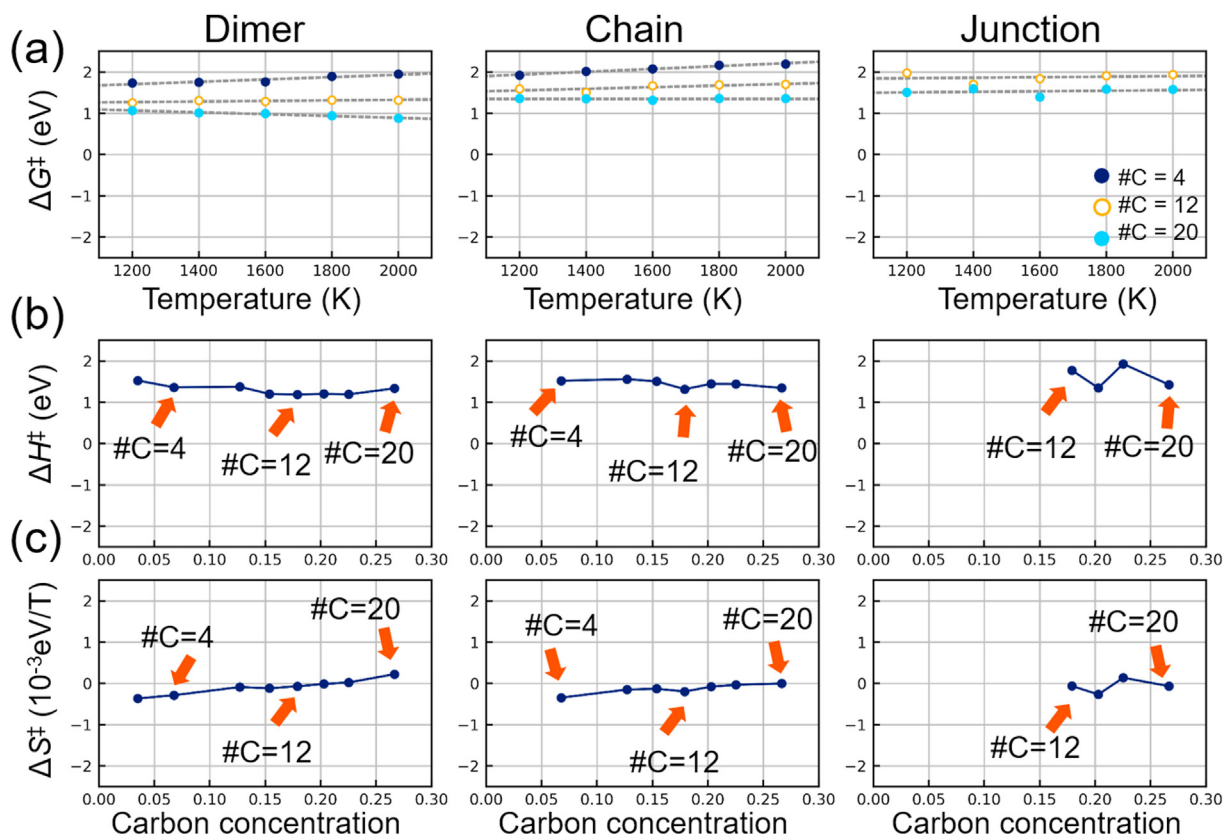
**Fig. 6.** (a) Activation free energy of the reaction of dimer formation, chain formation and junction formation with respect to temperature for nanoparticles with 4, 12 and 20 carbon atoms. Dashed lines represent the fitting line for each case. (b) Activation enthalpy and (c) activation entropy of the reaction of dimer formation, chain formation and junction formation with respect to carbon concentration. (A colour version of this figure can be viewed online.)
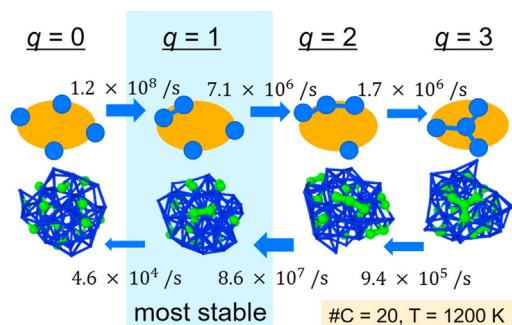


**Fig. 7.** Reaction rate coefficients between each state for 20 carbon, 1200 K case. The state of $q = 1$ is most stable. (A colour version of this figure can be viewed online.)

possible to analyze the segregation from bulk. The tendency that segregation becomes preferred and the entropic barrier of dimer formation decreases with increasing carbon concentration is expected to hold in larger systems as well although the effect of surface-volume ratio remains to be elucidated in future work. One limitation of method developed in this paper is that the reaction coordinate based on the maximum coordination number of carbon atoms cannot capture the long range order of the carbon network and can therefore not be applied to the formation of larger carbon structures. A second limitation of our employed CV is that it assumes a clear time scale separation between C—C dynamics and all other motions in the system, which might not be true in solid systems. More complex reaction coordinates may have to be derived for such cases. In future work, different types of reaction

coordinates must therefore be developed to describe the organization of segregated carbon into a hexagonal carbon network such as graphene and CNTs.

**CRediT authorship contribution statement**

**Satoru Fukuhara:** Conceptualization, Data curation, Formal analysis, Investigation, Methodology, Software, Validation, Visualization, Writing - original draft, Writing - review & editing. **Kristof M. Bal:** Conceptualization, Formal analysis, Investigation, Methodology, Software, Validation, Visualization, Writing - original draft, Writing - review & editing. **Erik C. Neyts:** Conceptualization, Funding acquisition, Methodology, Validation, Resources, Supervision, Writing - original draft, Writing - review & editing. **Yasushi Shibuta:** Conceptualization, Formal analysis, Funding acquisition, Investigation, Methodology, Resources, Supervision, Validation, Visualization, Writing - original draft, Writing - review & editing.

**Declaration of competing interest**

The authors declare that they have no known competing financial interests or personal relationships that could have appeared to influence the work reported in this paper.

## References

[1] G.R. Speich, W.C. Leslie, Tempering of steel, Metall. Trans. 3 (1972) 1043–1054.
[2] Y. Li, D. Raabe, M. Herbig, P.P. Choi, S. Goto, A. Kostka, et al., Segregation stabilizes nanocrystalline bulk steel with near theoretical strength, Phys. Rev. Lett. 113 (2014) 106104.
[3] C.H. Bartholomew, Carbon deposition in steam reforming and methanation, Catal. Rev. 24 (1982) 67–112.
[4] A. Reina, S. Thiele, X. Jia, S. Bhaviripudi, M.S. Dresselhaus, Growth of large-area single- and Bi-layer graphene by controlled carbon precipitation on poly-crystalline Ni surfaces, J. A. Schaefer and J. Kong, Nano Res 2 (2009) 509–516.
[5] R.S. Weatherup, H. Amara, R. Blume, B. Dlubak, B.C. Bayer, M. Diarra, et al., Interdependency of subsurface carbon distribution and graphene–catalyst interaction, J. Am. Chem. Soc. 136 (2014) 13698–13708.
[6] R.I. Babicheva, M. Dahanayaka, B. Liu, E.A. Korznikova, S.V. Dmitriev, M.S. Wu, et al., Characterization of two carbon allotropes, cyclicgraphene and graphe-nylene, as semi-permeable materials for membranes, Mater. Sci. Eng. B 259 (2020) 114569.
[7] H. Yoshida, S. Takeda, T. Uchiyama, H. Kohno, Y. Homma, Atomic-scale in-situ observation of carbon nanotube growth from solid state iron carbide nano-particles, Nano Lett. 8 (2008) 2082–2086.
[8] S. Fukuhara, F. Shimojo, Y. Shibuta, Conformation and catalytic activity of nickel–carbon cluster for ethanol dissociation in carbon nanotube synthesis: Ab initio molecular dynamics simulation, Chem. Phys. Lett. 679 (2017) 164–171.
[9] M. Singleton, P. Nash, The C-Ni (carbon-nickel) system, Bull. Alloy Phase Di-agrams 10 (1989) 121–126.
[10] B.J. Lee, On the stability of Cr carbides, Calphad 16 (1992) 121–149.
[11] R.I. Babicheva, S.V. Dmitriev, Y. Zhang, S.W. Kok, N. Srikanth, B. Liu, et al., Effect of grain boundary segregations of Fe, Co, Cu, Ti, Mg and Pb on small plastic deformation of nanocrystalline Al, Comput. Mater. Sci. 98 (2015) 410–416.
[12] O. Piqué, I.Z. Koleva, F. Viñes, H.A. Aleksandrov, G.N. Vayssilov, F. Illas, Sub-surface carbon: a general feature of noble metals, Angew. Chem. Int. Ed. 58 (2019) 1744–1748.
[13] B. Martínez, O. Piqué, H. Prats, F. Viñes, F. Illas, Towards understanding the role of carbon atoms on transition metal surfaces: implications for catalysis, Appl. Surf. Sci. 513 (2020) 145765.
[14] Y. Shibuta, S. Maruyama, Molecular dynamics simulation of formation process of single-walled carbon nanotubes by CCVD method, Chem. Phys. Lett. 382 (2003) 381–386.
[15] A.J. Page, H. Yamane, Y. Ohta, S. Irle, K. Morokuma, QM/MD simulation of SWNT nucleation on transition-metal carbide nanoparticles, J. Am. Chem. Soc. 132 (2010) 15699–15707.
[16] E.C. Neyts, Y. Shibuta, A.C.T. Van Duin, A. Bogaerts, Catalyzed growth of carbon nanotube with definable chirality by hybrid molecular dynamics- force biased Monte Carlo simulations, ACS Nano 4 (2010) 6665–6672.
[17] Y. Magnin, A. Zappelli, H. Amara, F. Ducastelle, C. Bichara, Size dependent phase diagrams of nickel-carbon nanoparticles, Phys. Rev. Lett. 115 (2015) 205502.
[18] S. Angioletti-Uberti, M. Ceriotti, P.D. Lee, M.W. Finnis, Solid-liquid interface free energy through metadynamics simulations, Phys. Rev. B 81 (2010) 125416.
[19] A. Laio, M. Parrinello, Escaping free-energy minima, Proc. Natl. Acad. Sci. U.S.A. 99 (2002) 12562.
[20] M. Iannuzzi, A. Laio, M. Parrinello, Efficient exploration of reactive potential energy surfaces using Car-Parrinello molecular dynamics, Phys. Rev. Lett. 90 (2003) 238302.
[21] A. Barducci, G. Bussi, M. Parrinello, Well-tempered metadynamics: a smoothly converging and tunable free-energy method, Phys. Rev. Lett. 100 (2008), 020603.
[22] P. Tiwary, M. Parrinello, From metadynamics to dynamics, Phys. Rev. Lett. 111 (2013) 230602.
[23] P. Tiwary, M. Parrinello, A time-independent free energy estimator for met-adynamics, J. Phys. Chem. B 119 (2015) 736–742.
[24] O. Valsson, P. Tiwary, M. Parrinello, Enhancing important fluctuations: rare events and metadynamics from a conceptual viewpoint, Annu. Rev. Phys. Chem. 67 (2016) 159–184.
[25] S. Fukuhara, K.M. Bal, E.C. Neyts, Y. Shibuta, Accelerated molecular dynamics simulation of large systems with parallel collective variable-driven hyper-dynamics, Comput. Mater. Sci. 177 (2020) 109581.
[26] H. Eyring, The activated complex in chemical reactions, J. Chem. Phys. 3 (1935) 107.
[27] J. Horiuti, On the statistical mechanical treatment of the absolute rate of chemical reaction, Bull. Chem. Soc. Jpn. 13 (1938) 210–216.
[28] E. Vanden-Eijnden, F.A. Tal, Transition state theory: variational formulation, dynamical corrections, and error estimates, J. Chem. Phys. 123 (2005) 184103.
[29] C. Hartmann, C. Schütte, Comment on two distinct notions of free energy, Phys. Nonlinear Phenom. 228 (2007) 59–63.
[30] K.M Bal, S. Fukuhara, Y. Shibuta, E.C. Neyts, Free energy barriers from biased molecular dynamics simulations, J. Chem. Phys 153 (2020) 114118.
[31] U. Khalilov, A. Bogaerts, E.C. Neyts, Atomic scale simulation of carbon nano-tube nucleation from hydrocarbon precursors, Nat. Commun. 6 (2015) 10306.
[32] J.E. Mueller, A.C.T. Van Duin, W.A. Goddard, Development and validation of ReaxFF reactive force field for hydrocarbon chemistry catalyzed by nickel, J. Phys. Chem. C 114 (2010) 4939–4949.
[33] G.J. Martyna, M.L. Klein, M. Tuckerman, Nos'e–hoover chains: the canonical ensemble via continuous dynamics, J. Chem. Phys. 97 (1992) 2635–2643.
[34] Y. Engelmann, A. Bogaerts, E.C. Neyts, Thermodynamics at the nanoscale: phase diagrams of nickel-carbon nanoclusters and equilibrium constants for phase transitions, Nanoscale 6 (2014) 11981–11987.
[35] S. Plimpton, Fast parallel algorithms for short-range molecular dynamics, J. Comput. Phys. 117 (1995) 1–19.
[36] G.A. Tribello, M. Bonomi, D. Branduardi, C. Camilloni, G. Bussi, Plumed 2: new feathers for an old bird, Comput. Phys. Commun. 185 (2014) 604–613.
[37] M. Salvalaglio, C. Perego, F. Giberti, M. Mazzotti, M. Parrinello, Molecular-dynamics simulations of urea nucleation from aqueous solution, Proc. Natl. Acad. Sci. U.S.A. 112 (2015). E6–E14.
[38] D.A. Gómez-Gualdrón, P.B. Balbuena, Characterization of carbon atomistic pathways during single-walled carbon nanotube growth on supported metal nanoparticles, Carbon N. Y. 57 (2013) 298–309.